

On the role of initial and boundary conditions in numerical simulations of accretion flows

De-Fu Bu^{1*}, Feng Yuan^{1†}, Maochun Wu^{1,2}, and Jorge Cuadra^{1,3}

¹*Key Laboratory for Research in Galaxies and Cosmology, Shanghai Astronomical Observatory, Chinese Academy of Sciences, 80 Nandan Road, Shanghai 200030, China*

²*Graduate School of the Chinese Academy of Sciences, Beijing 100039, China*

³*Departamento de Astronomía y Astrofísica, Pontificia Universidad Católica de Chile, Chile*

Accepted . Received ; in original form

ABSTRACT

We study the effects of initial and boundary conditions, taking two-dimensional hydrodynamical numerical simulations of hot accretion flow as an example. The initial conditions considered include a rotating torus, a solution expanded from the one-dimensional global solution of hot accretion flows, injected gas with various angular momentum distributions, and the gas from a large-scale numerical simulation. Special attention is paid to the radial profiles of the mass accretion rate and density. Both can be described by a power-law function, $\dot{M} \propto r^s$ and $\rho \propto r^{-p}$. We find that if the angular momentum is not very low, the value of s is not sensitive to the initial condition and lies within a narrow range, $0.47 \lesssim s \lesssim 0.55$. However, the value of p is more sensitive to the initial condition and lies in the range $0.48 \lesssim p \lesssim 0.8$. The diversity of the density profile is because different initial conditions give different radial profiles of radial velocity due to the different angular momentum of the initial conditions. When the angular momentum of the accretion flow is very low, the inflow rate is constant with radius. Taking the torus model as an example, we have also investigated the effects of inner and outer boundary conditions by considering the widely adopted “outflow” boundary condition and the “mass flux conservation” condition. We find that the results are not sensitive to these two boundary conditions.

Key words: accretion, accretion discs – hydrodynamics– black hole physics

1 INTRODUCTION

Hot accretion flows, such as advection-dominated accretion flows (ADAFs; Ichimaru 1977; Rees et al. 1982; Narayan & Yi 1994; 1995; Abramowicz et al. 1995; see Narayan, Mahadevan & Quataert 1998 and Kato, Fukue & Mineshige 1998 for reviews) are interesting because they are likely operating in low-luminosity active galactic nuclei (AGNs), including the supermassive black hole in our Galactic center, and hard and quiescent states of black hole X-ray binaries (see Narayan 2005; Yuan 2007; Narayan & McClintock 2008; Ho 2008; Yuan 2011 for reviews). Because of its widespread applications, the properties of hot accretion flows have been investigated intensively in the last decade. Hot accretion flows are originally proposed and studied analytically by vertically-integrated one-dimensional method (e.g., Narayan 1994). In the analytical works, the mass accretion rate is

usually assumed to be constant with radius. Under this assumption, the radial profile of density satisfies $\rho(r) \propto r^{-3/2}$.

Later on, intensive numerical simulation works have been performed to investigate the hot accretion flows. One of the most important finding is that the mass inflow rate is not a constant of radius; rather, it decreases inward. Correspondingly, the density profile flattens. The density profile obtained by the simulations is $\rho \propto r^{-p}$, with $0.5 \lesssim p \lesssim 1$. This is true for both hydrodynamic (HD) and magnetohydrodynamic (MHD) simulations (e.g., Stone, Pringle & Begelman 1999, hereafter SPB99; Igumenshchev & Abramowicz 1999, 2000, hereafter IA99, IA00; Stone & Pringle 2001; Hawley, Balbus & Stone 2001; Machida, Matsumoto & Mineshige 2001; Hawley & Balbus 2002; Igumenshchev, Narayan & Abramowicz 2003; Pen, Matzner & Wong 2003; De Villiers, Hawley & Krolik 2003; Yuan & Bu 2010; Pang, et al. 2011; McKinney, Tchekhovskoy & Blandford 2012; Li, Ostriker & Sunyaev 2013; see Yuan, Wu & Bu 2012 for a review). One model proposed to explain the above result is ADIOS (adiabatic inflow-outflow solution).

* E-mail:dfbu@shao.ac.cn

† E-mail:fyuan@shao.ac.cn

In this scenario, the inward decrease of inflow rate is because of mass lost via outflow (Blandford & Begelman 1999, 2004; Begelman 2012).

By analyzing the HD and MHD numerical simulation data, Yuan, Bu & Wu (2012, hereafter YBW2012; see also Li, Ostriker & Sunyaev 2013) show that outflow must exist, thus confirming the ADIOS scenario. Moreover, they investigated the physical mechanism of producing outflows. In the HD case, they find that the temperature of outflow is systematically higher than that of inflow (Fig. 8 in YBW2012). This suggests that the outflow is driven by the buoyancy which arises because of the convective instability of the HD accretion flow. In the case of MHD flow, they find that the specific angular momentum of outflow is close to the Keplerian angular momentum; while that of inflow is much lower (Fig. 11 in YBW2012). This suggests that it is the centrifugal force associated with the magnetic field that drives the outflow (Blandford & Payne 1982).

The radial profile of mass accretion rate (or density) is important because of the following reasons. The profile of mass accretion rate determines the emitted spectrum and other radiative features of an accretion flow (e.g., Quataert & Narayan 1999; Yuan, Quataert & Narayan 2003). With the increasing power of telescopes, the gas properties (density, temperature) at the Bondi radius of galaxies can be observed directly in some sources, such as Sgr A* and NGC 3115. Using the observational data and Bondi accretion theory (Bondi 1952), we can obtain the mass accretion rate at Bondi radius. Then depending on the radial profile of mass accretion rate (or more exactly the density), the radiation of the accretion flow is completely different. In cosmology simulations and other simulations studying the accretion flow on relatively large scale (e.g., Cuadra et al. 2005; 2006; 2008; Springel et al. 2005; Booth & Schaye 2009; Power et al. 2011; Hobbs et al. 2012), we can at most resolve the Bondi radius and determine the Bondi accretion rate. Then the mass accretion rate profile can determine the evolution of black hole mass and spin. The radial profile of mass accretion rate is also important to determine the feedback efficiency of an AGN. It is well known that feedback from AGN can strongly influence the physical properties of their vicinity, their host galaxies, and even of the intergalactic material of galaxy clusters to which they belong (e.g., Proga, Stone & Kallman 2000; Proga 2007; Kurosawa & Proga 2009; Ciotti & Ostriker 1997; 2001; 2007; Ciotti, Ostriker & Proga 2009; Novak, Ostriker & Ciotti 2011). Both the radiation and mass outflow from a AGN can influence its surroundings. The radiation from AGN can heat or cool the gas surrounding it, and the efficiency of heating or cooling depends on the spectrum and the conditions of the gas. The outflows can directly blow away the gas surrounding an AGN. If the Bondi accretion rate can be estimated from observations, the mass accretion rate profile within the Bondi radius can then determine how much radiation and outflow can be produced and further influence the environment of AGNs.

In this paper, we will study how the properties (especially radial profiles of mass accretion rate and density) of hot accretion flows depend on the initial and boundary conditions. Our motivations are as follows. In the realistic universe, the environment of accretion flows is likely very complex and differ from each other. Correspondingly, the initial

conditions of accretion flows, such as their radial velocity, temperature, and angular momentum, should be very different in different sources. In the literature, torus and injection models are usually adopted as the initial condition of simulations. YBW2012 studied several HD models. In their model A, the initial condition is a rotating torus. In model C, they inject gas at the outer boundary. Although the description and strength of viscosity are same in different models, the properties of the accretion flows are found to be quite different. First, in model A, the flow is nearly symmetric to the equatorial plane, with inflow being close to the equatorial plane ($\theta = 70^\circ - 90^\circ$ in a spherical coordinate) and outflow close to the surface of the disk ($\theta = 50^\circ$ and 140°). In model C, the flow is not symmetric to the equatorial plane, and large-scale bulk motions dominate the flow. Second, in model C, the radial velocity of inflow close to the equatorial plane can be described as $v_r \propto r^{-0.5}$; but in model A, the radial velocity scaling with radius is much steeper. The difference between the results obtained by different initial settings motivates us to systematically study the influence of the initial conditions on the properties of hot accretion flows.

In the present work, we focus on HD simulation. In reality, people now believe that it is the MHD turbulence associated with the magneto-rotational instability (MRI; Balbus & Hawley 1991; 1998) that is responsible for the angular momentum transfer in accretion flows. Therefore, MHD simulation is more realistic. Our considerations of adopting HD simulation are as follows. First, MHD simulation is obviously more expensive; and the results depend on the initial configuration and strength of the magnetic field. Second, in many astrophysical simulations such as large-scale cosmological ones, magnetic field is not considered and HD simulations are still the dominant ones. It is thus of practical usefulness to consider HD simulations. Third, we expect that if the initial and boundary conditions are important to determine some properties of HD accretion flow, it should also be important for MHD flows. Moreover, by comparing all relevant HD and MHD numerical simulations, Yuan, Wu & Bu (2012) found that the radial profiles of inflow rate obtained by various HD and MHD simulations are very similar. In other words, it seems that the result does not depend on the presence or absence of magnetic field, the strength and configuration of the magnetic field, and the dimension of calculation (two or three dimension). Such an apparently surprising result was predicted and explained in Begelman (2012). This implies that maybe the results obtained in the present study can be applied to MHD case as well.

The structure of the paper is as follows. In §2, we describe the basic equations, various initial and boundary conditions adopted and our numerical method. The results of simulations will be given in §3. We summarize our results in §4.

2 NUMERICAL METHOD

2.1 Equations

In spherical coordinates (r, θ, ϕ) , we solve the following hydrodynamical equations describing accretion:

$$\frac{d\rho}{dt} + \rho \nabla \cdot \mathbf{v} = 0, \quad (1)$$

$$\rho \frac{d\mathbf{v}}{dt} = -\nabla p - \rho \nabla \psi + \nabla \cdot \mathbf{T}, \quad (2)$$

$$\rho \frac{d(e/\rho)}{dt} = -p \nabla \cdot \mathbf{v} + \mathbf{T}^2/\mu, \quad (3)$$

Here, ρ , p , \mathbf{v} , ψ , e and \mathbf{T} are density, pressure, velocity, gravitational potential, internal energy and anomalous stress tensor, respectively. $d/dt (\equiv \partial/\partial t + \mathbf{v} \cdot \nabla)$ denotes the Lagrangian time derivative. We adopt an equation of state of ideal gas $p = (\gamma - 1)e$, and set $\gamma = 5/3$.

We use the stress tensor \mathbf{T} to mimic the shear stress, which is in reality magnetic stress associated with MHD turbulence driven by MRI. Following SPB99, we assume that the only non-zero components of \mathbf{T} are the azimuthal components,

$$T_{r\phi} = \mu r \frac{\partial}{\partial r} \left(\frac{v_\phi}{r} \right), \quad (4)$$

$$T_{\theta\phi} = \frac{\mu \sin \theta}{r} \frac{\partial}{\partial \theta} \left(\frac{v_\phi}{\sin \theta} \right). \quad (5)$$

This is because the MRI is driven only by the shear associated with orbital dynamics. Other components of the stress are much smaller than the azimuthal components (Stone & Pringle 2001). We adopt the coefficient of shear viscosity $\mu = \nu \rho$. We assume $\nu \propto r^{1/2}$, which is the usual “ α ” description. In all models, we set $\alpha=0.01$ to eliminate the discrepancy due to the magnitude of viscosity coefficient.

We use pseudo-Newtonian potential to mimic the general relativistic effects, $\psi = -GM/(r - 2r_g)$, where M is the center black hole mass, G is the gravitational constant and $r_g \equiv GM/c^2$ is the gravitational radius. The self gravity of the gas is neglected.

2.2 Models

For our aim, we adopt four kinds of initial conditions. In all our models, the inner boundaries locate at $r = 2.7r_g$. In the angular direction, the boundary conditions are set by symmetry at the poles. In model A1, at the outer radial boundary, we use mass-flux conservation boundary conditions (see Section 3.4); For the inner radial boundary in model A1, we use outflow boundary conditions. In all of other models, at the inner and outer radial boundaries, we use outflow boundary conditions.

In model A series, the initial condition of our simulation is an equilibrium torus with constant specific angular momentum given by (Papaloizou & Pringle 1984)

$$\frac{p}{\rho} = \frac{(\gamma - 1)GM}{\gamma R_0} \left[\frac{R_0}{r} - \frac{1}{2} \left(\frac{R_0}{r \sin \theta} \right)^2 - \frac{1}{2d} \right]. \quad (6)$$

Here, R_0 is the radius of the center (density maximum) of the torus, and d is the distortion of the torus. We assume $R_0 = 200r_g$ and $d = 1.25$ in our models. The maximum density of the torus $\rho_{max} = 1.0$. The specific angular momentum of the initial torus equals to the Keplerian angular momentum at the torus center. Initially, the torus is embedded in a low-density medium. The density and pressure of the medium are $\rho_m = 10^{-4}$ and $p_m = \rho_m/r$, respectively.

In model B, we use the one-dimensional steady global ADAF solution (G-ADAF-S; Yuan 1999) as our initial condition. Because this solution is one-dimensional, we extend it into two-dimensions in the following way. The values

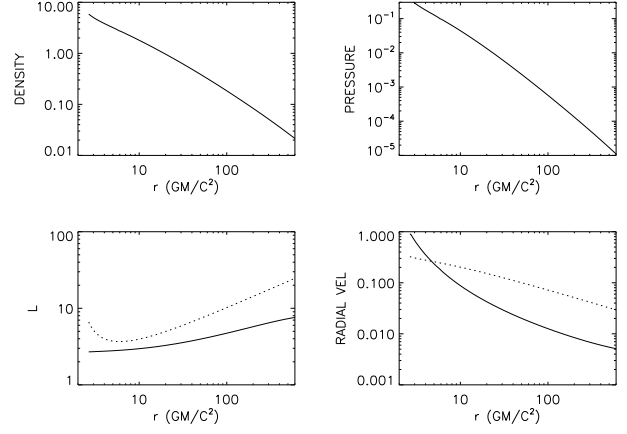


Figure 1. One-dimensional global solution of hot accretion flows on which the initial condition of Model B is based. The dotted line in the angular momentum plot shows the Keplerian one; the dotted line in the radial velocity plot shows the sound speed.

of $\rho(r, 0)$, $p(r, 0)$, $v_r(r, 0)$, $l(r, 0)$ are from the global solution of ADAF. The density and pressure of flow exponentially decreases along θ : $\rho(r, \theta) = \rho(r, 0) \exp(-z^2/2H^2)$, $p(r, \theta) = p(r, 0) \exp(-z^2/2H^2)$, where $z = r|\cos \theta|$. For simplicity, we set the radial velocity $v_r(r, \theta) = v_r(r, 0)$ and azimuthal velocity $v_\phi(r, \theta) = l(r, 0)/(r \sin \theta)$. Initially, the θ component of the velocity is set to 0. In Figure 1, we plot the radial structure of these initial quantities.

Model C series are “injection” type. The gas is continually injected into the computational domain from the outer boundary. The θ component of the velocity of the injected gas is set to be zero. The density of the injected gas has a Gaussian distribution about the equator $\rho(r, \theta) = \rho_{max} \exp[-0.5(\theta - \pi/2)^2]$, with $\rho_{max} = 1$. In model C series, we have assumed that the injected gas have different angular momentum, radial velocity and internal energy. The rotational and radial velocities of the injected gas are $v_\phi = f_\phi v_k$ and $v_r = f_r v_k$, respectively, with v_k being the Keplerian velocity at the injection radius. The internal energy of the injected fluid $e = f_e \rho \psi$. In models C1-C4, f_e is set to 0.2, so the gas in these models is marginally bound, i.e. the Bernoulli parameter $Be < 0$. The detailed parameters are listed in Table 1.

In model D, the initial condition is adopted to be more “realistic”. We inject gas in full-range of θ . The properties of the injected gas are taken from a parsec-scale, realistic SPH simulation of the gas dynamics around Sgr A* (see Cuadra et al 2006, 2008 for details). The gas in this simulation originates as stellar winds of young massive stars, whose orbital and mass-loss properties are well determined from observations (Paumard et al 2006; Martins et al 2007). Shocks between different stellar winds heat up the gas, creating a hot accretion flow. They ran the simulation for ~ 1000 yr, which corresponds to several orbital times for the stars that originate the gas. In order to apply the 3 dimensional data from the simulation by Cuadra (2008) to the current 2 dimensional simulation, we have to chose a symmetry axis – we take the vector normal to the plane on which most stellar orbits lie as the rotation axis. We then average the data over the azimuthal angle to obtain 2 dimension data. Then, the

Table 1. Models in this paper

Run	Descriptions	$N_r \times N_\theta$	$l(f_\phi^1)$	$v_r(f_r^2)$	$e(f_e^3)$	t_f	r_{out}	s^4	p^5
A	torus	168×88	0.9-1.1	0.0		4.5	$800r_g$	0.49	0.53
A1 ⁶	tours	168×88	0.9-1.1	0.0		4.5	$800r_g$	0.5	0.54
Ah1	torus	252×132	0.9-1.1	0.0		4.5	$800r_g$	0.49	0.52
Ah2	torus	336×176	0.9-1.1	0.0		4.5	$800r_g$	0.49	0.52
B	G-ADAF-S	200×88	0.4-0.8	0.01-1	0.2	10.	$600r_g$	0.55	0.8
C1	injection	168×88	0.95	0.1	0.2	900.	$600r_g$	0.53	0.51
C2	injection	168×88	0.55	0.1	0.2	900.	$600r_g$	0.54	0.49
C3	injection	168×88	0.55	0.01	0.2	900.	$600r_g$	0.55	0.48
C4	injection	168×88	0.25	0.1	0.2	900.	$600r_g$	0.54	0.63
C5	injection	168×88	0.1	0.1	2.0	900.	$600r_g$	0	1.31
C6	injection	168×88	0.1	0.1	4.0	900.	$600r_g$	0	1.3
D [†]	injection	168×88	0.6	0.01-0.1	0.1	600.	$600r_g$	0.47	0.65

1, f_ϕ is the ratio of angular momentum to the local Keplerian angular momentum for the initial tours or injected gas.

2, f_r is the ratio of radial velocity to the local Keplerian velocity for the initial tours or injected gas.

3, f_e is the ratio of the internal energy to the local gravitational energy for the initial torus or the injected gas.

4, s is the power law index of the radial profile of inflow rate.

5, p is the power law index of the radial profile of density.

6, In model A1, at the outer radial boundary, we use mass-flux conservation boundary conditions.

[†] The properties of the injected gas in model D are more "realistic".

2 dimensional data was used as initial conditions in model D presented in this work. Looking at these data, we find the average specific angular momentum of the gas at the inner boundary of their simulation ($5000r_g$) is $l \approx 0.6l_k$. The radial velocity has large fluctuation, and is $\sim 0.01 - 0.1v_k$. The temperature is $\sim 7 \times 10^7$ K. We use the method of least squares with equation $\log(y) = a + b * \log(r)$ (y denotes the physical quantities such as specific energy, angular momentum and radial velocity) to fit the results of Cuadra et al. (2008). After we obtain the value of a and b , we can extrapolate the result of Cuadra et al. to obtain the physical quantities used at the outer boundary ($600r_g$) in model D.

Table 1 summarizes the properties of the models mentioned-above. Column (2) gives a brief description of the models (initial state is torus, global ADAF solution or injection from the outer boundary). Column (3) shows the numerical resolution. Columns (4)-(6) show the properties of the gas in the initial conditons. They are the specific angular momentum compared to the local Keplerian angular momentum, the radial velocity compared to the local Keplerian velocity, the specific internal energy compared to the local gravitational energy. Column (7) gives the final time at which we stopped the simulation (in units of the Keplerian orbital time at $r = 200 r_g$). Column (8) denotes the outer boundary. When the simulations achieve steady state, the power-law index of the radial profiles of mass inflow rate and density are given in columns (9) and (10), respectively.

2.3 Numerical method

We use the ZEUS-2D code (Stone & Norman 1992a,1992b) to solve equations (1)-(3). We adopt non-uniform grid in the radial direction $(\Delta r)_{i+1}/(\Delta r)_i = 1.037$. Similarly, we adopt non-uniform angular zones with $(\Delta \theta)_{j+1}/(\Delta \theta)_j = 0.9826$ for $0 \leq \theta \leq \pi/2$ and $(\Delta \theta)_{j+1}/(\Delta \theta)_j = 1.0177$ for $\pi/2 \leq \theta \leq \pi$.

3 RESULTS

Following SPB99, we define the mass inflow and outflow rates, \dot{M}_{in} and \dot{M}_{out} , as follows,

$$\dot{M}_{in}(r) = 2\pi r^2 \int_0^\pi \rho \min(v_r, 0) \sin \theta d\theta \quad (7)$$

$$\dot{M}_{out}(r) = 2\pi r^2 \int_0^\pi \rho \max(v_r, 0) \sin \theta d\theta \quad (8)$$

The net mass accretion rate is,

$$\dot{M}_{acc}(r) = \dot{M}_{in}(r) + \dot{M}_{out}(r) \quad (9)$$

In a turbulent accretion flow, there are real outflows and turbulent outflows. Real outflow means that the flows are systematically outward moving gas. Turbulent outflow means that the outflow is not real outflow but an outward moving portion of a turbulent eddy. In equation 8, the outflow rate calculated include both real outflows and turbulent outflows. Thus, the outflow rate calculated using equation 8 is an upper limit of real outflows. The main result of YBW2012 is that they show that systematic real outflow must be significant and may even dominate the outflow rate calculated in eq. 8. This result is confirmed by a more recent work (Yuan et al. in preparation). In this work, they try to follow the trajectory of some tracer particles to judge how strong the real outflow is. They confirm the result of YBW2012.

Usually people use the sign of Bernoulli parameter to judge whether the outflow can escape to infinity or not. We must point out, however, that in a viscous or an MHD flow, the Bernoulli parameter is not constant. Both the viscosity and magnetic field can change the value of Bernoulli parameter during their motion. Moreover, as shown in YBW2012, the initial condition of the simulations is important to determine the Bernoulli parameter of outflows. If the Bernoulli parameter of the initial gas is negative, i.e., they are bound, the outflow will usually be bound as well. This is the case of Model A in YBW2012. On the other hand, if the Bernoulli

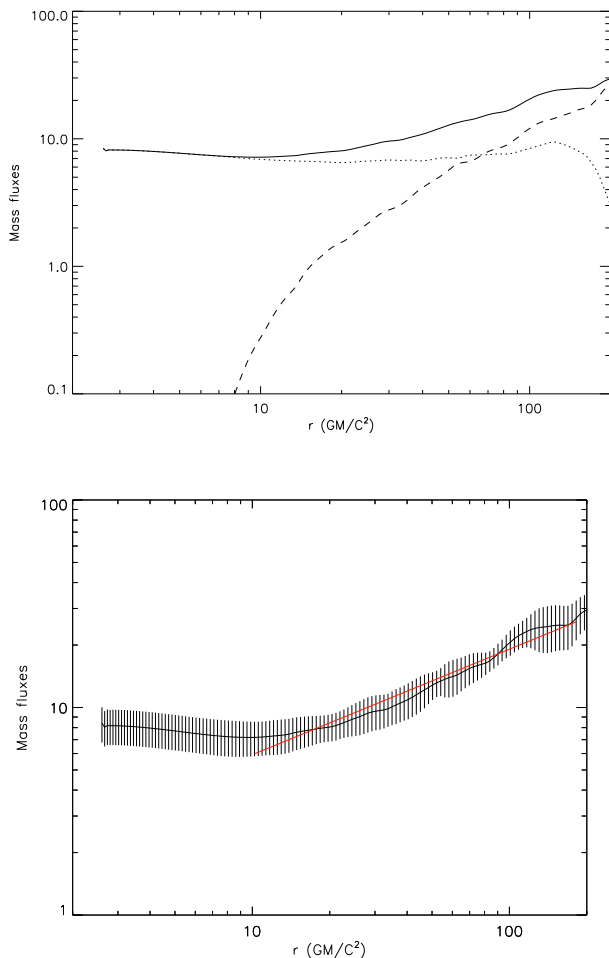


Figure 2. Top: The radial profile of the time-averaged and angle integrated mass inflow rate \dot{M}_{in} (solid line), outflow rate \dot{M}_{out} (dashed line), and the net rate \dot{M}_{acc} (dotted line) in model A. They are defined in equations (7), (8), and (9), respectively. Bottom: Power law fit to the inflow rate. The red line is our fit to the time-averaged inflow rate. The black line is the time-averaged inflow rate. In this panel, we also show the standard deviation of the time-averaged inflow rate.

parameter of the initial gas is positive, as in the case of Model C in that work, the outflows are unbound (see Fig. 4 in YBW2012).

3.1 Torus model

In Figure 2, the top panel plots the time-averaged (from 4-4.5 orbits) and angle-integrated mass accretion rate in model A. The radial profile of the inflow rate from $10r_g$ to $200r_g$ can be described by

$$\dot{M}_{in} = \dot{M}_{in}(r_{out}) \left(\frac{r}{r_{out}} \right)^{0.49}, \quad (10)$$

while it is almost constant within $10r_g$. The initial condition and the description of viscosity in model A are same as those in “Run K” of SPB99. The radial profile obtained in SPB99 is $\dot{M}_{in} \propto r^{3/4}$, steeper than ours. The discrepancy is because the coefficient of viscosity in our model is 10 times larger

than that in “Run K” of SPB99 (IA99; SPB99; Yuan, Wu & Bu 2012).

The bottom panel of Figure 2 shows our fit to the time-averaged inflow rate. The standard deviation of the time-averaged inflow rate is also shown. We can see that it is not large. We have tested the standard deviation of time-averaged physical quantities (e.g. mass inflow rate, density, pressure and angular momentum) in other models and found that it is not large.

Figure 3 shows the radial structure of the time-averaged (from 4-4.5 orbits) flow near the equatorial plane in model A. The black lines correspond to the average over angle between $\theta = 84^\circ$ to $\theta = 96^\circ$. The red lines correspond to the average over angle between $\theta = 78^\circ$ to $\theta = 102^\circ$. The radial scalings of physical variables obtained over angle integral between $\theta = 84^\circ$ to $\theta = 96^\circ$ are almost identical to those obtained over angle integral between $\theta = 78^\circ$ to $\theta = 102^\circ$. We conclude that it is safe to measure the radial scalings by angle integral from $\theta = 84^\circ$ to $\theta = 96^\circ$. We have done test for other models and find same conclusion. McKinney & Gammie (2002) also find that averaging over $\theta = 72^\circ$ to $\theta = 108^\circ$ produces nearly identical results with those averaging over $\theta = 84^\circ$ to $\theta = 96^\circ$.

From the inner boundary to $200r_g$, the density, gas pressure, angular momentum can be described by a power law scaling with radius,

$$\rho \propto r^{-0.53}, p \propto r^{-1.64}, l \propto r^{0.31}. \quad (11)$$

This density profile is significantly flatter than that obtained in Yuan, Wu & Bu (2012) where they got $\rho \propto r^{-0.85}$. This is because in that work the initial torus is put at a much larger radius, $R_0 = 10^4 r_g$. Thus, the radial dynamical range of Yuan, Wu & Bu (2012) is much larger than the present work and the results suffer little from the plunging flow close to the black hole. The density profile is similar to that obtained in SPB99, where they found $\rho \propto r^{-0.5}$. The numerical setting in SPB99 is different from that in this paper, SPB99 adopt Newtonian potential and $\alpha = 10^{-3}$. The former inclines to make the density profile steeper while the latter inclines to make it flatter. The rough consistency between SPB99 and the present work is because the two effects cancel each other.

3.2 Model B

In model B, our initial condition is based on the one-dimensional global ADAF solution (G-ADAF-S). The radial structure of our initial conditions is shown in Fig. 1. One feature is that the angular momentum of the flow is smaller than that of the torus model. Fig. 4 shows the time-averaged (from 800-900 orbits) and angle-integrated mass accretion rate of model B. The radial profile of the inflow rate from $10r_g$ to $200r_g$ can be described by

$$\dot{M}_{in} = \dot{M}_{in}(r_{out}) \left(\frac{r}{r_{out}} \right)^{0.55}. \quad (12)$$

Again, the accretion rate within $10r_g$ is almost constant. The result is approximately consistent with Model A.

Figure 5 displays the radial structure of the time-averaged (from 800-900 orbits) flow near the equatorial plane (between $\theta = 84^\circ$ to $\theta = 96^\circ$). From the inner bound-

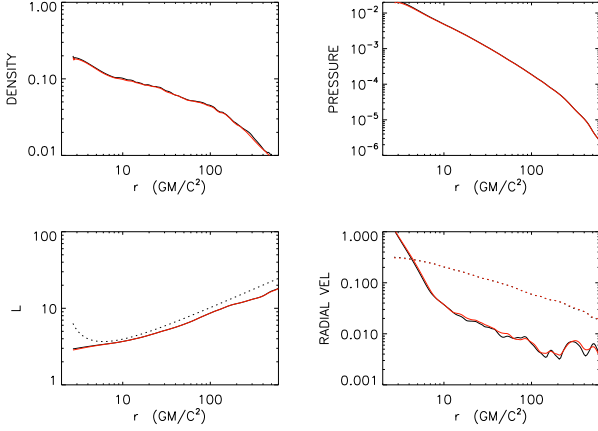


Figure 3. Radial profiles of some quantities in model A. The black lines correspond to those averaged over the polar angle between $\theta = 84^\circ$ to $\theta = 96^\circ$. The red lines correspond to those averaged over the polar angle between $\theta = 78^\circ$ to $\theta = 102^\circ$. The dotted line in the lower-left plot corresponds to the Keplerian angular momentum. The dotted lines in the lower-right plot corresponds to the sound speed.

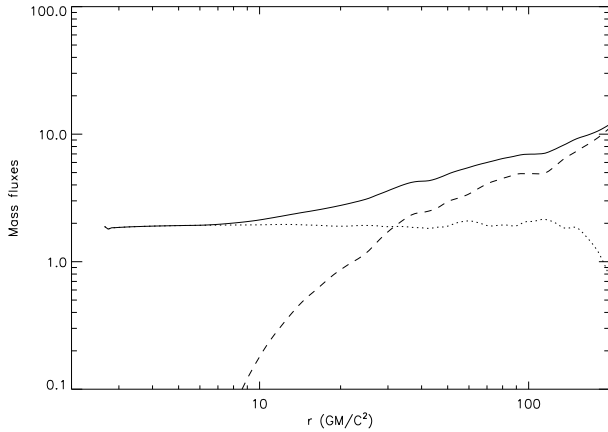


Figure 4. Same with the top panel of Fig. 2, but for model B.

ary to $200r_g$, the density, gas pressure, angular momentum can be described by,

$$\rho \propto r^{-0.8}, p \propto r^{-1.65}, l \propto r^{0.26}. \quad (13)$$

We see that the density profile is much steeper than that in model A. We can understand it as follows. Because of the initial condition, in the outer region (close to $200r_g$), the angular momentum in model A is much higher than that of model B; therefore, the radial velocity in model A is much smaller than that of model B. Close to the black hole, in both models, the radial velocity is equal to light speed. The radial profile of velocity in model A is steeper than that of model B. Given that mass accretion rate have comparable power-law index, the steeper radial velocity profile in model A results in flatter density profile.

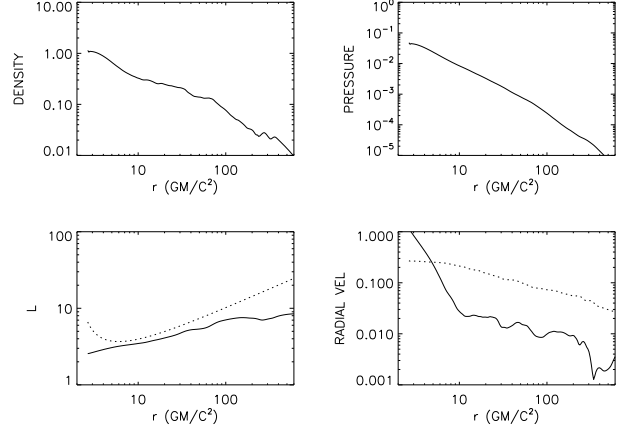


Figure 5. Same with Fig. 3, but for model B.

3.3 Injection models

3.3.1 Injection models with large and moderate angular momentum

We first define the circularization radius r_c as

$$\sqrt{\left(\frac{r_c}{r_{out}}\right)} = \frac{l_{inj}}{l_{ok}}, \quad (14)$$

where r_{out} is our outer boundary, l_{inj} and l_{ok} are the angular momentum of the injected gas and the Keplerian angular momentum at r_{out} , respectively. When $l_{inj} \ll l_{ok}$, the injected gas will quickly infall until it get close to the circularization radius. Because the gas pressure gradient force is important in hot accretion flow, the effective circularization radius (hereafter, ECR), where the gas stops quick infall, may be 2 ~ 3 times bigger than r_c .

Fig. 6 shows the mass accretion rates in models C1 ~ C4 while Fig. 7 shows the time averaged physical quantities near the equator (between $\theta = 84^\circ$ to $\theta = 96^\circ$). In model C4, the circularization radius $r_c \approx 37.5r_g$. Because of the pressure gradient force, the ECR of gas locates at $\sim 100r_g$. Beyond ECR, we see that the angular momentum and inflow rate are both approximately constant. The reason why the inflow rate is constant is that convection is weak and the accretion timescale is short (refer to §3.3.2 for more details). In model C4, quasi-steady state is achieved within $50r_g$, the mass accretion rate from 10 to $50r_g$ can be described by

$$\dot{M}_{in} = \dot{M}_{in}(r_{out}) \left(\frac{r}{r_{out}}\right)^{0.54}. \quad (15)$$

From the inner boundary to $50r_g$, the density, gas pressure, angular momentum can be described by,

$$\rho \propto r^{-0.63}, p \propto r^{-1.31}, l \propto r^{0.2}. \quad (16)$$

The circularization radii of the gas in models C1 and C2 are $541.5r_g$ and $181.5r_g$, respectively. The mass inflow rates of models C1 and C2 from $10r_g$ to $200r_g$ can be described as

$$\dot{M}_{in} \propto r^{0.53}, \dot{M}_{in} \propto r^{0.54}, \quad (17)$$

respectively. The density, pressure, and angular momentum of Model C1 and C2 can be described by,

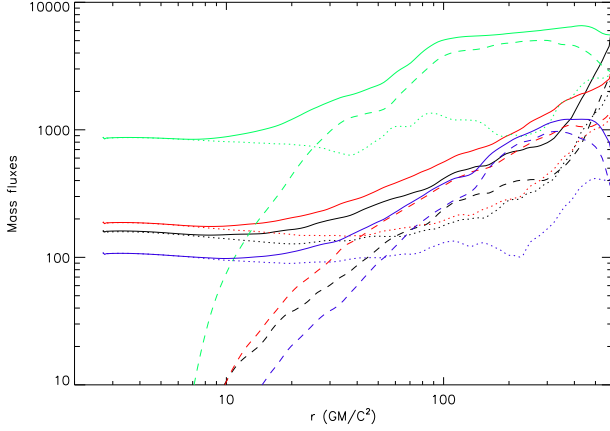


Figure 6. Same with the top panel of Fig. 2, but for model C1 (black line), C2 (red line), C3 (blue line), and C4 (green line).

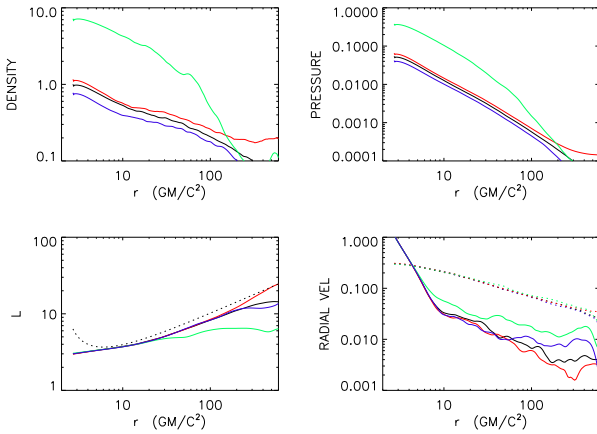


Figure 7. Same with Fig. 3, but for model C1 (black line), C2 (red line), C3 (blue line) and C4 (green line).

$$\rho \propto r^{-0.51}, p \propto r^{-1.32}, l \propto r^{0.31}, \quad (18)$$

and

$$\rho \propto r^{-0.49}, p \propto r^{-1.31}, l \propto r^{0.33}, \quad (19)$$

respectively.

In order to investigate the effects of injected radial velocity, we carry out model C3. The only difference between models C2 and C3 is that the injected radial velocity in C3 is 10 times smaller than that in model C2. Compared to model C2, the mass accretion rate close to the black hole in C3 is slightly smaller (by a factor smaller than 2), the profile of inflow rate is slightly steeper, while the slopes of density, pressure and angular momentum in model C3 almost remain same. We thus conclude that the effects of radial velocity of the injected gas are small.

In models C1 \sim C4, the properties of the injected gas are “artificially” given. In Model D, we adopt a “realistic” initial condition, i.e., the properties of the injected gas are taken from the large-scale simulations of Sgr A* (Cuadra 2008). Figs. 8 & 9 show the profiles of accretion rates and physical quantities near the equator (between $\theta = 84^\circ$ to $\theta = 96^\circ$). The results are

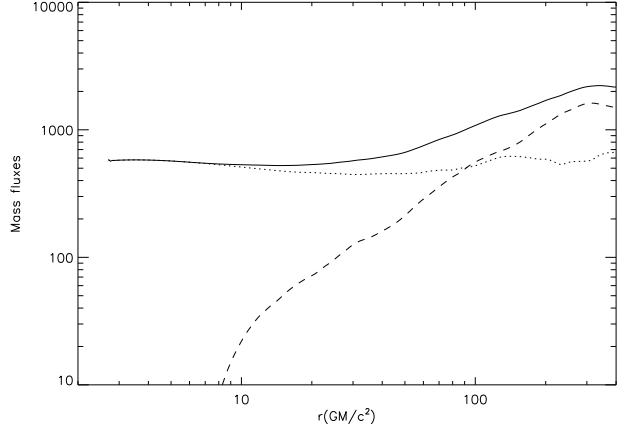


Figure 8. Same with the top panel of Fig. 2, but for model D.

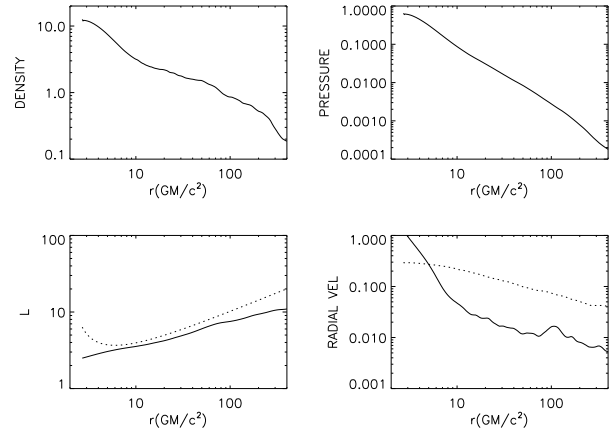


Figure 9. Same with Fig. 3, but for model D.

$$\dot{M}_{\text{in}} \propto r^{0.47}, \quad (20)$$

$$\rho \propto r^{-0.65}, p \propto r^{-1.57}, l \propto r^{0.34}. \quad (21)$$

3.3.2 Injection models with very low angular momentum

Previous analytical works found that when the angular momentum of the flow is smaller than a critical value, the accretion pattern is Bondi-like, i.e., the sonic radius is large, no matter the flow is inviscid (Abramowicz & Zurek 1981) or viscous (Yuan 1999). Proga & Begelman (2003, hereafter, PB2003) studied inviscid accretion flow and found that when the angular momentum of the flow is smaller than the Keplerian angular momentum at $16r_g$, the gas inside the Bondi radius has a constant accretion rate. Because viscosity is neglected in PB2003, there is no heating for the gas, the entropy of the gas is constant with radius. Therefore the flow in PB2003 is convectively stable. When viscous heating is included, the entropy of gas should increase inwards and convection may play some role on the mass accretion rate profile. It is interesting then to investigate whether in this case the mass accretion rate is constant.

In models C5 and C6, the injected angular momentum of the gas equals the Keplerian angular momentum at

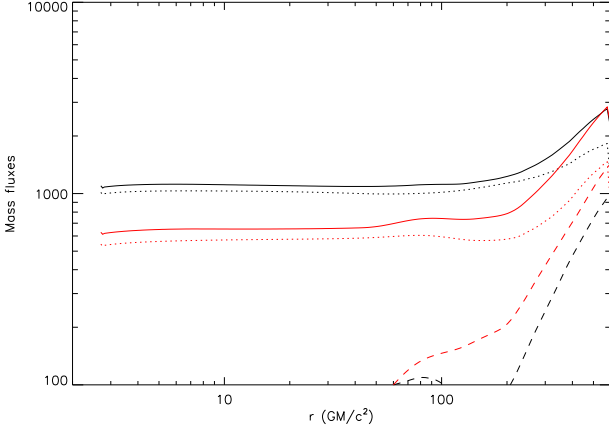


Figure 10. Same with the top panel of Fig. 2, but for model C5 (black line) and C6 (red line).

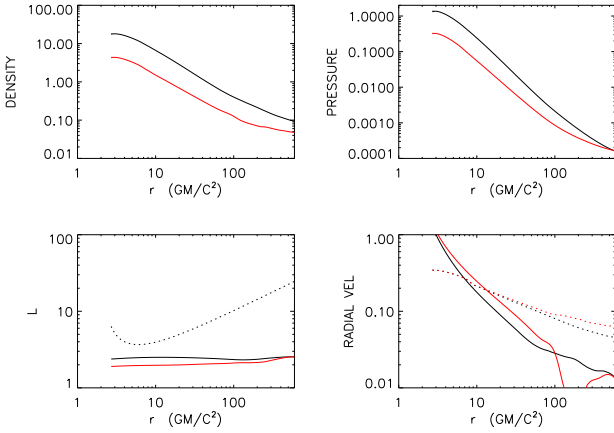


Figure 11. Same with Fig. 3, but for model C5 (black line) and C6 (red line).

$6r_g$. In models C5 and C6, the temperature of the injected gas is higher than Virial temperature, so the Bondi radius $R_B = GM/c_\infty$ (where c_∞ is the sound speed at infinity) is smaller than the outer boundary, $R_B \approx 300r_g$ and $150r_g$, respectively. In reality, R_B is usually much larger.

Figures 10 and 11 show the radial profiles of mass accretion rates and some quantities near the equator near the equator (between $\theta = 84^\circ$ to $\theta = 96^\circ$) in models C5 and C6. The results are

$$\dot{M} \approx \text{const.} \quad (22)$$

for both models, and correspondingly, the density profile is close to the analytical Bondi result,

$$\rho \propto r^{-1.31}, \rho \propto r^{-1.3}, \quad (23)$$

for models C5 and C6. The decrease of mass accretion rate close to the outer boundary is not physical but due to boundary effects.

We analyze that the reason for a constant accretion rate is because convection is very weak. The condition for convective instability in a rotating accretion flow is:

$$N_{\text{eff}}^2 \equiv N^2 + \sigma^2 = -\frac{1}{\rho} \frac{dP}{dR} \frac{d \ln(P^{1/\gamma}/\rho)}{dR} + \sigma^2 < 0, \quad (24)$$

where N is the usual Brunt-Väisälä frequency and σ is the epicyclic frequency which is equal to rotation angular velocity Ω for nearly Keplerian rotation (Narayan & Yi 1994). For a non-rotating flow, $\sigma = 0$, this condition is then equivalent to an inward increase of entropy, which is the well-known Schwarzschild criterion. In the accretion process, the inward increase of entropy is because of viscous heating. The viscous heating rate is proportional to square of gradient of angular velocity. In models C5 and C6, the gradient of angular velocity is very small. Therefore, viscous heating rate is very small in models C5 and C6, which results in a small entropy gradient in models C5 and C6. The first term in equation (24) is proportional to gradient of entropy. We find in almost half computational domain the flow is convectively stable according to equation (24). In addition, the accretion timescale of the flow in models C5 and C6 is very small. We find that only in a very small region around $100r_g$, the growth timescale of convection is slightly smaller than the gas accretion timescale. This is why convection is unimportant¹.

3.4 Effects of boundary conditions

In numerical simulations, for the radial boundaries, the outflow boundary conditions are usually adopted. This condition means that the hydrodynamical variables (e.g. density, velocity, pressure) are directly copied from the first (or last) active zone to the ghost zone. In spherical coordinate, the mass flux is expressed as $r^2 \rho v_r$. If we use outflow boundary conditions, the gradient of mass flux is not zero at radial boundaries, thus there may be artificial mass accumulation. In order to avoid this problem, some authors use mass-flux conservation boundary condition which assumes that the gradient of mass flux cross the boundaries is zero.

We have studied how these two boundary conditions affect the properties of accretion flow in the torus model. For the inner radial boundary, we find that the properties of the flows are very insensitive to the inner boundary conditions. The reason is that at the inner boundary, the flow is supersonic, so no wave signal can transfer back to affect the properties of the flow (McKinney & Gammie 2002). In order to study how the two boundary conditions at the outer radial boundary affect the properties of the flow, we carry out model A1. The only difference between models A1 and A is the outer radial boundary conditions. In models A1 and A, we use mass-flux conservation boundary condition and outflow boundary condition, respectively. Fig. 12 plots the time-averaged (from 4-4.5 orbits) and angle integrated mass accretion rate in the two models. Fig. 13 shows the radial structure of the time-averaged flow near the equatorial plane ($\theta = 84^\circ$ to $\theta = 96^\circ$) in the two models. From Fig. 12 and Fig. 13, we find that the properties of the flow are very insensitive to the outer boundary conditions.

¹ In the MHD simulation of Bondi accretion flow, under some initial configuration of the magnetic field, Igumenshchev & Narayan (2002) find significant magnetic reconnection heating thus entropy production. In this case, the flow is convectively unstable and $\rho \propto r^{-0.5}$.

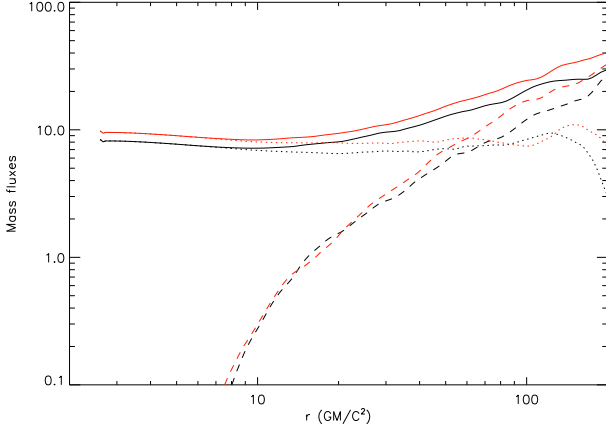


Figure 12. Same with the top panel of Fig. 2, but for models A (black lines) and A1 (red lines).

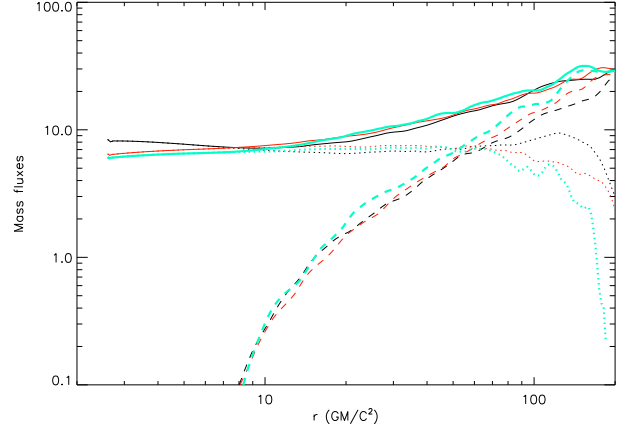


Figure 14. Same with the top panel of Fig. 2, but for model A (black lines) and Ah1 (red lines) and Ah2 (green lines).

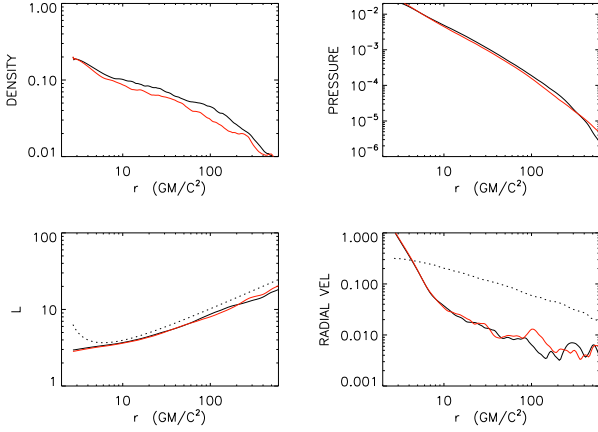


Figure 13. Same with Fig. 3, but for models A (black lines) and A1 (red lines).

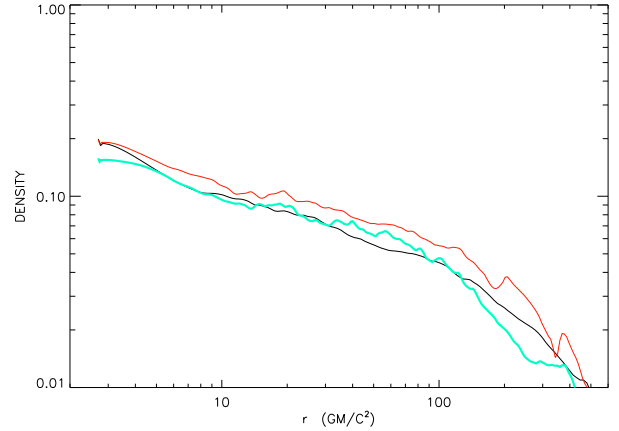


Figure 15. Radial profiles of density in models A (black line) and Ah1 (red line) and Ah2 (green line). The quantity has been averaged over time and the polar angle between $\theta = 84^\circ$ to $\theta = 96^\circ$.

3.5 Dependence on resolution

In order to test whether the results obtained in this paper depend on resolution, we carry out models Ah1 and Ah2. For model Ah1, the numbers of grids in r and θ directions are 1.5 times those in model A. In model Ah2, the resolution is 2 times higher than that in model A.

Fig. 14 plots the time-averaged (from 4-4.5 orbits) and angle integrated mass accretion rate in models A (black lines) and Ah1 (red lines) and Ah2 (green lines). From this figure, we can see that the power-law indexes of the inflow rate in torus models with different resolution are almost same. Fig. 15 shows the radial structure of the time-averaged density near the equatorial plane ($\theta = 84^\circ$ to $\theta = 96^\circ$) in models A (black line) and Ah1 (red line) and Ah2 (green line). The radial scaling of density with different resolution is also almost same. From Fig. 14 and Fig. 15, we find that the resolution used in most of the models (168×88) in this paper is enough.

4 SUMMARY

In this paper, we have investigated the effects of initial and boundary conditions on the properties of hot accretion flow using two-dimensional hydrodynamic simulations. We have considered several initial conditions, including the most widely adopted “torus” and “injection” conditions, and the more realistic flow properties from large-scale simulation. Special attention is paid to the radial profiles of mass accretion rate and density. Both profiles can be described by a power-law function ($\dot{M}_{\text{in}} \propto r^s, \rho \propto r^{-p}$). The simple description to different initial conditions and the corresponding power-law index are summarized in Table 1.

The most interesting result is that for various initial conditions, if the angular momentum of the accretion flow is not too low so that a rotationally supported accretion flow can form beyond $10r_g$, the power-law index of the radial profile of inflow rate s lies in a narrow range of $0.47 \lesssim s \lesssim 0.55$. But on the other hand, the radial profile of density is more sensitive to the initial condition. The power-law index p lies in a wider range $0.48 \lesssim p \lesssim 0.8$. Given that the inflow rate

profile is almost same for various initial conditions, the diversity of the density profile is because different initial conditions give different angular momentum profiles and thus different radial velocity profiles. Then it is an interesting question why different initial conditions give roughly same inflow rate profile. The readers are referred to Begelman (2012) for an explanation.

Since $\dot{M} \propto r^2 v_r \rho(r)$, for hot accretion flows, we usually expect $p = 1.5 - s$, if $v_r \propto r^{-0.5}$ according to the self-similar scaling law of hot accretion flows (e.g. Narayan & Yi 1994). We note that our results do not satisfy $p = 1.5 - s$, but smaller than this value. This is partly because the density profile depends not only on the inflow rate profile, but also on outflow rate profile, which is much steeper. Another reason is that $v_r \propto r^{-0.5}$ is not well satisfied since the flow is close to the black hole.

If the angular momentum of the flow is very low (i.e., models C5 and C6), we find that inside the Bondi radius, the mass accretion rate is almost constant. Physically, this is because convection is very weak, thus, very little outflow is produced. In these models, the viscous heating rate is very small due to the small angular velocity gradient. Small viscous heating rate results in a very small gradient of entropy, thus, convection is weak. In addition, the accretion timescale is very small.

We have also studied the effects of boundary conditions. We have considered two widely adopted inner and outer boundary conditions, which are “outflow” boundary condition and “mass flux conservation” boundary condition. We have found that the properties of the flow are very insensitive to the radial boundary conditions.

5 ACKNOWLEDGMENTS

This work was supported in part by the Natural Science Foundation of China (grants 11103059, 11121062, and 11133005), the National Basic Research Program of China (973 Program 2009CB824800), and the CAS/SAFEA International Partnership Program for Creative Research Teams. J. C. acknowledges support from FONDECYT (11100240) and Basal (PFB0609). The simulations were carried out at Shanghai Supercomputer Center.

REFERENCES

- Abramowicz M. A., Zurek W. H., 1981, *ApJ*, 246, 314
 Abramowicz M. A., Chen X., Kato S., Lasota J. P., Regev O., 1995, *ApJ*, 438, L37
 Balbus S. A., Hawley J. F., 1991, *ApJ*, 376, 214
 Balbus S. A., Hawley J. F., 1998, *Rev. Mod. Phys.*, 70, 1
 Begelman M., 2012, *MNRAS*, 420, 2912
 Bondi H, 1952, *MNRAS*, 112, 195
 Booth C. M., Schaye J., 2009, *MNRAS*, 398, 53
 Blandford R., Payne D. G., 1982, *MNRAS*, 199, 883
 Blandford R., Begelman M., 1999, *MNRAS*, 303, L1
 Blandford R., Begelman M., 2004, *MNRAS*, 349, 68
 Ciotti L., Ostriker J. P., 1997, *ApJ*, 487, L105
 Ciotti L., Ostriker J. P., 2001, *ApJ*, 551, 131
 Ciotti L., Ostriker J. P., 2007, *ApJ*, 665, 1038
 Ciotti L., Ostriker J. P., Proga D., 2009, *ApJ*, 699, 89
 Cuadra J., Nayakshin S., Springel V., Di Matteo T., 2005, *MNRAS*, 360, L55
 Cuadra J., Nayakshin S., Springel V., Di Matteo T., 2006, *MNRAS*, 366, 358
 Cuadra J., Nayakshin S., Martins F., 2008, *MNRAS*, 383, 458
 De Villiers J. P., Hawley J. F., Krolik J. H., 2003, *ApJ*, 599, 1238
 Hawley J. F., Balbus S. A., Stone J. M., 2001, *ApJ*, 554, L49
 Hawley J. F., Balbus S. A., 2002, *ApJ*, 573, 738
 Ho L., 2008, *ARA&A*, 46, 475
 Hobbs A., Power C., Nayakshin S., King A. R., 2012, *MNRAS*, 421, 3443
 Ichimaru S., 1977, *ApJ*, 214, 840
 Igumenshchev I. V., Abramowicz M. A., 1999, *MNRAS*, 303, 309
 Igumenshchev I. V., Abramowicz M. A., 2000, *ApJS*, 130, 463
 Igumenshchev I. V., Narayan R., 2002, *ApJ*, 566, 137
 Igumenshchev I. V., Narayan R., Abramowicz M. A., 2003, *ApJ*, 592, 1042
 Kato S., Fukue J., Mineshige S., 1998, *Black Hole Accretion Disks*. Kyoto Univ. Press, Kyoto
 Kurosawa R., Proga D., 2009, *MNRAS*, 397, 1791
 Li J., Ostriker J., Sunyaev R., 2013, *ApJ*, in press (arXiv:1206.4059)
 Machida M., Matsumoto R., Mineshige S., 2001, *PASJ*, 53, L1
 McKinney J. C., Gammie C. F., 2002, *ApJ*, 573, 728
 Martins F., Genzel R., Hillier D. J., Eisenhauer F., Paumard T., Gillessen S., Ott T., Trippe S., 2007, *A&A*, 468, 233
 McKinney J., Tchekhovskoy A., Blandford R., 2012, *MNRAS*, 423, 3083
 Narayan R., Yi I., 1994, *ApJ*, 428, L13
 Narayan R., Yi I., 1995, *ApJ*, 452, 710
 Narayan R., 2005, *Ap&SS*, 300, 177
 Narayan R., McClintock J.E., 2008, *New Astron. Rev.*, 51, 733
 Narayan R., Mahadevan R., Quataert E., 1998, in Abramowicz M. A., Bjornsson G., Pringle J. E., eds, *Theory of Black Hole Accretion Disks*. Cambridge Univ. Press, Cambridge, p. 148
 Novak G. S., Ostriker J. P., Ciotti L., 2011, *ApJ*, 737, 26
 Papaloizou J. C. B., Pringle J. E., 1984, *MNRAS*, 208, 721
 Pang B., Pen U.-L., Matzner C. D., Green S. R., Liebendorfer M., 2011, *MNRAS*, 415, 1228
 Paumard T., Genzel R., Martins F. et al., 2006, *ApJ*, 643, 1011
 Pen U. L., Matzner C. D., Wong S., 2003, *ApJ*, 596, L207
 Proga D., Stone J. M., Kallman T. R., 2000, *ApJ*, 543, 686
 Proga D., 2007, *ApJ*, 661, 693
 Proga D., Begelman M. C., 2003, *ApJ*, 582, 69
 Power C., Nayakshin S., King A., 2011, *MNRAS*, 412, 269
 Quataert E., Narayan R., 1999, *ApJ*, 520, 298
 Rees M. J., Begelman M. C., Blandford R. D., Phinney E. S., 1982, *Nat*, 295, 17
 Springel V., Di Matteo T., Hernquist L., 2005, *MNRAS*, 361, 776
 Stone J.M., Norman M. L., 1992a, *ApJS*, 80, 753
 Stone J.M., Norman M. L., 1992b, *ApJS*, 80, 791
 Stone J. M., & Pringle J. E., 2001, *MNRAS*, 322, 461
 Stone J. M., Pringle J. E., & Begelman M. C. 1999, *MNRAS*, 310, 1002
 Yuan F., 1999, *ApJ*, 521, L55
 Yuan F., Quataert E., Narayan R., 2003, *ApJ*, 598, 301
 Yuan F., 2007, in Luis C. Ho., Jian-Min Wang, eds, *ASP Conf. Ser.*, Vol.373, *The Central Engine of Active Galactic Nuclei*. Astron. Soc. Pac., San Francisco, p.95
 Yuan F., 2011, *ASP Conf. Ser.* 439, *The Galactic Center: a Window to the Nuclear Environment of Disk Galaxies*, ed. Mark R. Morris, Q. Daniel Wang, and Feng Yuan, 346
 Yuan F., Bu D., 2010, *MNRAS*, 408, 1051
 Yuan F., Bu D., Wu M., 2012, *ApJ*, 761, 130
 Yuan F., Wu M., Bu D., 2012, *ApJ*, 761, 129